Journal of
Applied
Crystallography
ISSN 0021-8898

Received 8 October 2009
Accepted 4 March 2010

Modeling of kinematic diffraction from a thin silicon film illuminated by a coherent, focused X-ray nanobeam

Andrew Ying,[a] Braxton Osting,[a] I. C. Noyan,[a]* Conal E. Murray,[b] Martin Holt[c] and Jörg Maser[c]

[a]Columbia University, Department of Applied Physics and Applied Mathematics, New York, NY 10027, USA, [b]IBM T. J. Watson Research Center, Yorktown Heights, NY 10598, USA, and [c]Center for Nanoscale Materials, Argonne National Laboratory, Argonne, IL 60439, USA. Correspondence e-mail: icn2@columbia.edu

A rigorous model of a diffraction experiment utilizing a coherent, monochromatic, X-ray beam, focused by a Fresnel zone plate onto a thin, perfect, single-crystal layer is presented. In this model, first the coherent wave emanating from an ideal zone plate equipped with a direct-beam stop and order-sorting aperture is computed. Then, diffraction of the focused wavefront by a thin silicon film positioned at the primary focal spot is calculated. This diffracted wavefront is propagated to the detector position, and the intensity distribution at the detector plane is extracted. The predictions of this model agree quite well with experimental data measured at the Center for Nanoscale Materials nanoprobe instrument at Sector 26 of the Advanced Photon Source.

© 2010 International Union of Crystallography
Printed in Singapore – all rights reserved

1. Introduction

Current X-ray nanodiffractometers use X-ray beams with diameters in the range 25–50 nm (Chu *et al.*, 2008; Mimura *et al.*, 2007; Schroer *et al.*, 2005; Maser, Stephenson, Shu *et al.*, 2004). True nanometre-sized (<10 nm) beams are expected in the near future (Maser, Stephenson, Vogt *et al.*, 2004; Kang *et al.*, 2008; Yan, 2009). These beams are very divergent (of the order of milliradians for wavelengths of ~1 Å) and necessarily have high spatial coherence, as coherent illumination is required to achieve diffraction-limited resolution from optical systems. When such a wavefront is used for diffraction analysis of crystalline materials, computation of the resulting scattering pattern requires an accurate representation of the spatial and angular incident-beam distribution at the sample, a proper model of the scattering mechanism(s) within the sample, and propagation of the resulting coherent wavefront from sample to detector (Yan *et al.*, 2008).

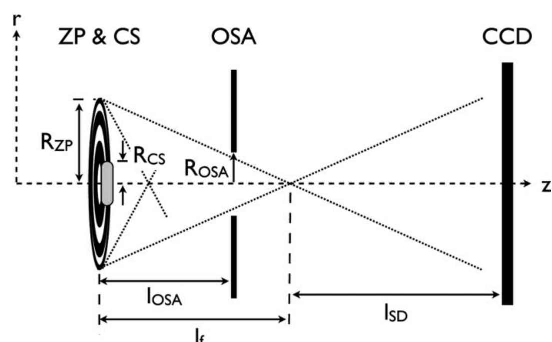

Figure 1
Schematic of a beamline with a Fresnel zone plate (ZP) focusing optic. A central stop (CS) is attached to the ZP to stop the zeroth-order beam. The dotted lines represent the focusing of the wavefield for the first- and third-order focal spots. An order-sorting aperture (OSA) is placed close to the primary focal spot to choose the focus diffraction order. The sample is placed at the primary focal spot.

An accurate model of the incident beam on the sample surface must incorporate all optical components encountered by the incident wavefront before impinging on the sample. In this paper we model Fresnel phase zone plates (ZPs), which to date have achieved the highest spatial resolution in the hard X-ray range. ZPs consist of concentric zones with alternating susceptibilities so that the amplitude and phase of the incident wave is modulated in these alternating zones. Diffraction of the incident wave produces multiple orders of focii along the axis of the ZP, and the desired focus is chosen by an order-sorting aperture (OSA), as in Fig. 1. A significant fraction of the direct beam passes undiffracted through the ZP. This is prevented from reaching the sample by using a central stop (CS) and an OSA. These additional optical components also modify the incident-beam distribution.

Several recent studies (Yan *et al.*, 2008; Kohn & Kazimirov, 2007; Kazimirov *et al.*, 2009) have modeled the diffracted waves excited by coherently focused incident X-ray beams from single crystals. Yan *et al.* (2008) considered the incident beam as a point source emitting a spherical wave, and modeled the evolution of the diffracted wave from a perfect or weakly deformed single-crystal sample. Kohn & Kazimirov (2007) modeled a topographic technique in which an ideal Gaussian X-ray beam focused by a parabolic refractive lens was diffracted in the Bragg geometry from a single-crystal substrate–epitaxial layer composite, and the one-dimensional

(linear) distribution of intensity with position was recorded by a detector placed at the focus of the lens. In an extension of this technique, Kazimirov *et al.* (2009) used a Fresnel zone plate to focus the beam and a CCD detector to record the two-dimensional diffraction image from silicon-on-insulator thin films. The cross section of the measured data at the diffraction plane showed qualitative agreement with the model calculations of one-dimensional intensity variations with spatial position. Each of these models treat relatively simple incident-beam profiles and use one-dimensional formulations to calculate the spatial variation of scattered intensity. To our knowledge, there have been no models that account for the full focused wavefield expected from a Fresnel zone plate defined by a set of vendor-supplied specifications or the two-dimensional topographic images that would be observed when the diffracted beam from a single-crystal sample illuminated by such an incident focused beam is recorded by a two-dimensional detector. In this paper we address these issues.

In what follows, a diffraction experiment utilizing a phase zone plate focusing optic and a CCD detector is modeled. In this model the Fresnel diffraction formula is used to calculate the complete focused wavefield emanating from an ideal phase zone plate. The simulation incorporates the effects of the central stop and the order-sorting aperture. Using this incident beam and kinematic scattering theory, the diffracted wave from a thin, perfect, Si layer placed at the first-order focal spot is calculated. This wave is then propagated to a two-dimensional detector, and the intensity pattern that would be recorded is constructed. The incident- and diffracted-beam computations are then compared with experimental data measured with the Center for Nanoscale Materials (CNM) Hard X-ray Nanoprobe at Sector 26-ID-C of the Advanced Photon Source (APS).

2. Theory

To simulate the diffracted wavefield from a thin film illuminated with a convergent, coherent nanobeam, we follow the method outlined by Yan *et al.* (2008). This framework uses the theories of free-space wave propagation and crystal diffraction, both of which are well known (Goodman, 1996; Authier, 2002). They are briefly reviewed here to establish notation.

2.1. Fresnel wave propagation

We define the Fresnel diffraction integral operator by

$$\mathcal{R}_z[f](\mathbf{x}) = \begin{cases} (f * g_z)(\mathbf{x}), & z > 0, \\ f(\mathbf{x}), & z = 0, \end{cases} \qquad (1)$$

where $g_z(\mathbf{x})$ is the convolution kernel

$$g_z(\mathbf{x}) = \frac{\exp(2\pi i k z)}{i\lambda z} \exp\left(\frac{i\pi k}{z}|\mathbf{x}|^2\right).$$

If we consider $U_0(\mathbf{x})$ to be a monochromatic, scalar, electromagnetic field (with wavelength $\lambda = 1/k$) measured at an aperture, the wavefield at a distance z from the aperture, $U_z(\mathbf{x})$, can be described in the Fresnel approximation by $U_z(\mathbf{x}) = \mathcal{R}_z[U_0](\mathbf{x})$ (Goodman, 1996). We interchangeably use 'aperture function' and wavefield at $z = 0$ throughout. For a radially symmetric aperture function $f(\mathbf{x}) = f(\rho)$, we rewrite equation (1) in polar coordinates, and integrate over the angular coordinate to yield the simpler expression

$$\mathcal{R}_z[f](r) = 2\pi \frac{\exp(2\pi i k z)}{i\lambda z} \exp\left(i\frac{\pi k}{z} r^2\right) \times \int_0^\infty f(\rho) \exp\left(i\frac{\pi k}{z}\rho^2\right) J_0\left(\frac{2\pi}{\lambda z} r\rho\right) \rho \, \mathrm{d}\rho, \qquad (2)$$

where J_0 is the zeroth-order Bessel function of the first kind. The integral in equation (2) may be referred to as the Hankel transform of order zero or the radial Fourier transform. In this paper, we will use the uniqueness property of the Fresnel diffraction integral, which can be stated as $\mathcal{R}_{z_1+z_2} f = \mathcal{R}_{z_1}\mathcal{R}_{z_2} f$ for all $z_1,\ z_2 \geq 0$.

In the Fraunhofer approximation, the wavefield a distance z from the aperture is written

$$U_z(\mathbf{x}) = \frac{1}{i\lambda z} \exp(2\pi i k z) \exp\left(i\frac{\pi k}{z}|\mathbf{x}|^2\right) \mathcal{F}[U_0]\left(\frac{\mathbf{x}}{\lambda z}\right), \qquad (3)$$

where $\mathcal{F}[f](\mathbf{k}) = \int f(\mathbf{x}) \exp(-2\pi i \, \mathbf{k} \cdot \mathbf{x}) \, \mathrm{d}\mathbf{x}$ is the Fourier transform. This approximation is valid when the (dimensionless) Fresnel number, $F = a^2/(\lambda z)$, is small ($F \ll 1$), where a is the characteristic width of the aperture function (Goodman, 1996). Following Yan *et al.* (2008), we can also define an angular Fresnel number, $Y_\mathrm{A} = \alpha^2 z/\lambda$, where α is the characteristic width of the Fourier transform of the aperture function. The far-field approximation is valid when $Y_\mathrm{A} \gg 1$.

2.2. X-ray diffraction from a thin film

To model diffraction from a thin film, we consider a kinematically scattering sample with structure factor $F_\mathbf{h}$ and reciprocal lattice vector $\mathbf{h}$. The diffracted angular spectrum $A_h(\mathbf{k}_\mathrm{i}, \mathbf{k}_\mathrm{d})$ for a unit plane wave with wavevector $\mathbf{k}_\mathrm{i}$ and diffracted wavevector $\mathbf{k}_\mathrm{d}$ is given by

$$A_h(\mathbf{k}_\mathrm{i}, \mathbf{k}_\mathrm{d}) = (F_\mathbf{h}/v_\mathrm{c}) \int_V \exp(2\pi i \Delta\mathbf{k}_\mathbf{h} \cdot \mathbf{x}) \, \mathrm{d}\mathbf{x}, \qquad (4)$$

where v_c is the unit-cell volume, V is the crystal domain and $\Delta\mathbf{k}_\mathbf{h} \equiv \mathbf{k}_\mathrm{d} - \mathbf{k}_\mathrm{i} - \mathbf{h}$ (Authier, 2002). When $\Delta\mathbf{k}_\mathbf{h} = 0$, the Bragg condition is satisfied and the diffracted intensity exhibits a maximum. We note that, for equation (4) to be valid, the thickness of the (single-crystal) thin film along the diffraction vector must be smaller than the extinction depth, t_e, of the material. For films appreciably thicker than t_e, dynamical diffraction formulations (Yan *et al.*, 2007) must be used.

Let us consider a thin film with thickness t_f in the $\hat{\mathbf{z}}$ direction, and infinite in the $\hat{\mathbf{x}}\hat{\mathbf{y}}$ plane. Furthermore, let us assume that the crystal and sample coordinate systems are aligned such that $\mathbf{h}$ and $\hat{\mathbf{z}}$ are antiparallel. In this case, the integrals in the $\hat{\mathbf{x}}$ and $\hat{\mathbf{y}}$ directions in equation (4) are Dirac δ functions, yielding

$$A_h(\mathbf{k}_\mathrm{i}, \mathbf{k}_\mathrm{d}) \propto \delta(\Delta k_{hx})\,\delta(\Delta k_{hy}) \int_0^{t_\mathrm{f}} \exp(i2\pi\Delta k_{hz} z)\, \mathrm{d}z \propto \delta(\Delta k_{hx})\,\delta(\Delta k_{hy}) \,\mathrm{sinc}\{\pi(k_{\mathrm{d}z} + k_{\mathrm{i}z} - h_z)t_\mathrm{f}\}. \qquad (5)$$

Table 1
Numerical values used in the simulations.

The zone plate and central stop are both gold; the order-sorting aperture is platinum–iridium.

Instrument	
E	11.2 keV
λ	1.107×10^{-10} m
k	9.033×10^{9} m^{-1}
Zone plate	
N_{ZP}	1385
R_{ZP}	66.5×10^{-6} m
Δr	24×10^{-9} m
l_f	28.8346×10^{-3} m
n	$1 - (2.3193 \times 10^{-5} - 1.4665 \times 10^{-6}i)$
t_{ZP}	300×10^{-9} m
φ_{ZP}	$-(0.1257 - 0.0079i)\pi$
Central stop	
R_{CS}	30×10^{-6} m
t_{CS}	80×10^{-6} m
φ_{CS}	$-(33.5219 - 2.1196i)\pi$
Order-sorting aperture	
R_{OSA}	15×10^{-6} m
l_{OSA}	25.8347×10^{-3} m
CCD	
l_{SD}	700 mm

In a traditional radial scan (*i.e.* scans along $\mathbf{h}$) of a symmetric reflection for a thin film, $\Delta k_{hx} = \Delta k_{hy} = 0$ and $k_{dz} + k_{iz} - h_z = 2(\sin\theta - \sin\theta_B)/\lambda$, where θ is the angle between the incident beam and the sample surface, and θ_B is the Bragg angle of the reflection. The diffracted intensity is given by

$$I(\Delta 2\theta) \propto |A_h|^2 \propto \mathrm{sinc}^2(\pi t_f \cos\theta_B \Delta 2\theta/\lambda), \qquad (6)$$

where $\Delta 2\theta = 2\theta - 2\theta_B$. Equation (6) predicts a central peak bracketed by fringe peaks.[1] The FWHM of the diffraction peak, β_t, can be calculated from equation (6), which yields the classical Scherrer equation (Ying *et al.*, 2009)

$$\beta_t \simeq \frac{0.886\lambda}{t_f \cos\theta_B}. \qquad (7)$$

The radial scan is also sensitive to the lattice strain, ε, along $\mathbf{h}$. The strain is measured as a peak shift $\Delta 2\theta$ relative to θ_B and is given by

$$\varepsilon = \frac{\sin\theta_B}{\sin(\theta_B + \Delta\theta)} - 1, \qquad (8)$$

where $\Delta\theta = \Delta 2\theta/2$. It is important to note that the angular coordinate 2θ (thus β_t and $\Delta 2\theta$) is measured with respect to the incident wavevector $\mathbf{k}_i$.

3. Simulations

In this section, we compute the spatial intensity distributions using the equations from §2. Numerical values used in the calculations are tabulated in Table 1. These values were selected to match the experimental settings that are described in §4.

3.1. Incident-beam simulation

We consider a monochromatic plane wave of unit amplitude in the hard X-ray spectrum incident on an ideal Fresnel ZP. The ZP consists of alternating concentric rings of material (zones) of decreasing width. Light passing through odd zones is given a phase shift $\varphi_{ZP} = (2\pi/\lambda)(n-1)t_{ZP}$, where n is the index of refraction and t_{ZP} is the thickness of the ZP (Jones, 1969). This is an idealization of the 'staggered spoke' zone plate structure used in the experiment and described by Feng *et al.* (2007). Each zone is bounded between radii given by $\{(m-1/2)\lambda l_f\}^{1/2} \le r \le \{(m+1/2)\lambda l_f\}^{1/2}$ for $0 < m \le N_{ZP}$, where m is the integer order of the zone and N_{ZP} is the order of the outermost zone. For the $m = 0$ zone, $0 \le r \le (\lambda l_f/2)^{1/2}$. Thus, the wavefield measured in the aperture of the ZP is

$$U_{ZP}(r) = \begin{cases} \exp(i\varphi_{ZP}) & \text{for odd zones,} \\ 1 & \text{for even zones,} \\ 0 & \text{for } r \ge \{(N_{ZP}+1/2)\lambda l_f\}^{1/2}. \end{cases} \qquad (9)$$

A central stop with radius R_{CS} is attached to the ZP and the X-rays propagate through this region with an additional phase shift φ_{CS}. The composite aperture function is

$$U_0(r) = \begin{cases} U_{ZP}(r)\exp(i\varphi_{CS}) & \text{for } r < R_{CS}, \\ U_{ZP}(r) & \text{otherwise,} \end{cases} \qquad (10)$$

with $\varphi_{CS} = (2\pi/\lambda)(n-1)t_{CS}$, where t_{CS} is the thickness of the central stop.

To calculate the wavefield downstream of the OSA, we need to first calculate the wavefield at the OSA, U_{OSA}, by applying the radially symmetric Fresnel diffraction integral operator [equation (2)] to U_0 in equation (10). The one-dimensional integral in equation (2) is piecewise smooth over each zone and computed using a recursive adaptive Simpson quadrature rule. Because of the thickness and material of the OSA, it effectively truncates the wavefield for $r > R_{OSA}$ so, at the downstream side of the OSA, we have

$$U_{OSA}(r) = \begin{cases} \mathcal{R}_{l_{OSA}}[U_0](r) & \text{for } r < R_{OSA}, \\ 0 & \text{otherwise.} \end{cases} \qquad (11)$$

The subscript OSA on the field U is a label, while the subscript (l_{OSA}) on the Fresnel operator $\mathcal{R}$ is the distance of propagation. We now use the uniqueness property of the Fresnel integral operator to continue the beam from the OSA to the focal spot or past the focal spot to the CCD detector. This integral in equation (2) was simply calculated using the trapezoid rule with a 0.05 nm discretization.

This two-step wave propagation process was used to generate a plot of the amplitude downstream of the ZP, and the log of the amplitude is plotted in Fig. 2(*a*). The simulation shows that the central portion of the straight-through beam is blocked by the central stop. Most of the incident beam is seen to pass straight through the ZP, while the diffracted wavefield converges for multiple orders of focii. The focal order is

[1] This result is the manifestation of the *Pendellösung* effect in this formulation of the diffracted intensity.

selected by the order-sorting aperture, which is placed at $z = l_{\rm OSA}$ for the primary focus spot. Here, only the focused wavefield within the radius of the OSA is allowed to propagate through. We note the Fresnel approximation used in this simulation is invalid for z near the ZP and OSA, and the scattering at the OSA is a result of this approximation.

The field at the focal spot is given by

$$U_{\rm f}(r) = \mathcal{R}_{l_{\rm f}-l_{\rm OSA}}[U_{\rm OSA}](r), \qquad (12)$$

with the amplitude plotted in Fig. 2(*b*). The simulation shows an intensity FWHM of 22.4 nm, slightly smaller than the Rayleigh resolution $1.22\Delta r = 30$ nm, where Δr is the outermost zone width. This complex wavefield at the focal spot $U_{\rm f}$ is used in §3.2 to simulate diffraction from a kinematically scattering thin film.

As seen in Fig. 2(*a*), the focused incident beam diverges from the focal spot as it propagates to the CCD detector. The wavefield at the CCD detector is

$$U_{\rm CCD}(\mathbf{x}) = \mathcal{R}_z[U_{\rm OSA}](r), \qquad (13)$$

where $z = l_{\rm f} - l_{\rm OSA} + l_{\rm SD}$ is the distance from the OSA to the detector. In Fig. 3(*a*) we plot the computed radial incident wavefield intensity, normalized to the integrated intensity in the nonzero region. The calculation uses a 1 µm step size at the CCD and averages the intensity over 13 µm regions to emulate CCD pixels. Our simulations show that these oscillations are a consequence of the truncation of the wavefield by

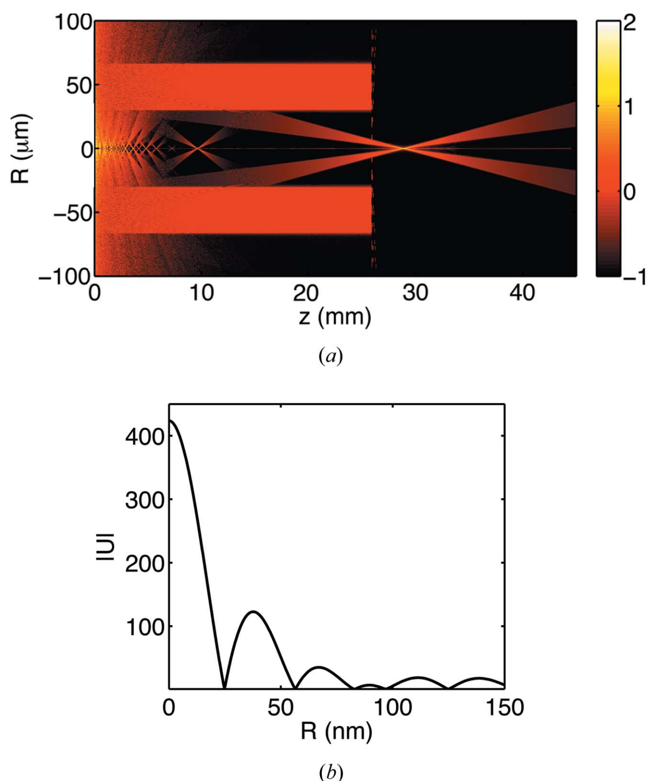

Figure 2
(*a*) Log of the amplitude of the wavefield generated from the ZP with the CS and OSA considered. The OSA is at $z \simeq 26$ mm. The primary focus of the ZP is seen at $z \simeq 29$ mm, with the divergent cone of radiation propagating to large z. A central line of amplitude (two orders of magnitude smaller than the focused amplitude) can be seen as a result of the zone plate used in the model. (*b*) The amplitude of the wavefield at the primary focal spot.

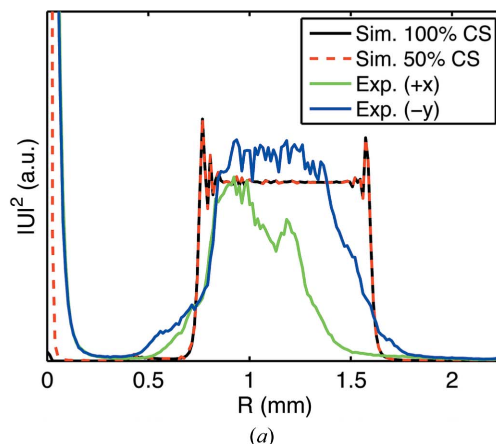

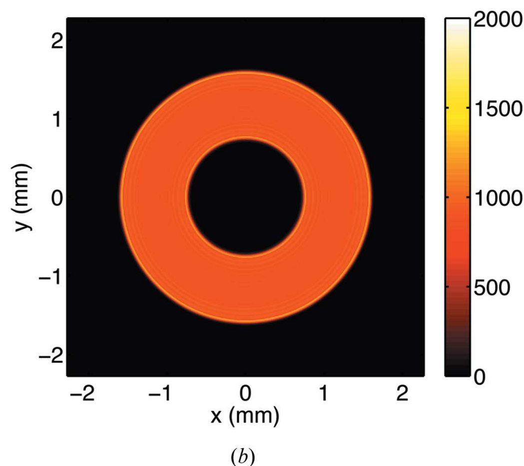

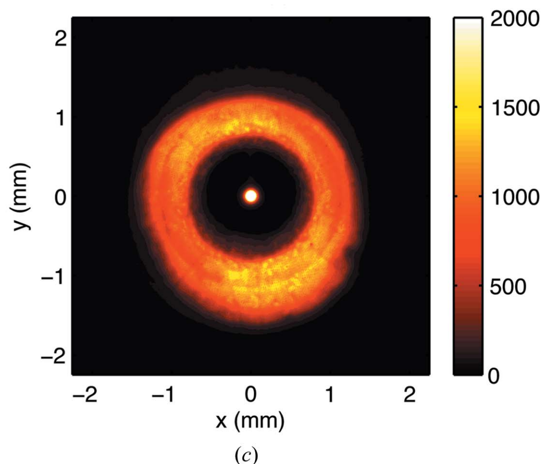

Figure 3
(*a*) The radial intensity distribution of the incident beam at the detector plane ($z = 700$ mm): computed (black and red), experimental (green and blue). Using a central stop with half the thickness of the ideal central stop (dashed red), a peak in intensity at $R = 0$ is reproduced in the simulation. (*b*) A simulated CCD image of the incident-beam intensity. (*c*) The measured incident-beam intensity at the CCD. Slices of the radial intensity distribution along $+\hat{\mathbf{x}}$ and $-\hat{\mathbf{y}}$ are plotted in (*a*) in green and blue, respectively. Leakage from the central stop, seen in the center of the annulus, saturated the CCD detector. The simulated plots are normalized to the integrated intensity of the nonzero annulus. The experimental plots are normalized to the integrated intensity of the slice along $-\hat{\mathbf{y}}$.

the OSA, a physical realization of Gibb's phenomena for truncated Fourier series. In Fig. 3(*b*), we show the simulated CCD image based on this calculated radial distribution. The simulation shows a ring of intensity resulting from the incident wave being limited in the center by the CS.

3.2. Thin-film diffraction simulation

A general wavefield incident on a sample, $U_{\rm i}(\mathbf{x})$, may be decomposed into its angular spectrum by the Fourier transform $A_{\rm i}(\mathbf{k}) = \mathcal{F}[U_{\rm i}](\mathbf{k})$. Each plane-wave component of the incident beam excites a diffracted plane wave, which interferes coherently with all other diffracted waves resulting from the other incident plane-wave components (Yan *et al.*, 2008). Thus, the diffracted amplitude for a particular wavevector $\mathbf{k}'_{\rm d}$ can be written as an integral over all components of the incident angular spectrum,

$$A(\mathbf{k}'_{\rm d}) = \int A_{\rm i}(\mathbf{k}'_{\rm i})\, A_h(\mathbf{k}'_{\rm i}, \mathbf{k}'_{\rm d})\, {\rm d}\mathbf{k}'_{\rm i}, \qquad (14)$$

where $\mathbf{k}'_{\rm d}$ and $\mathbf{k}'_{\rm i}$ are two-dimensional wavevectors defined in the sample coordinate system. It should be noted here that, while $A_h(\mathbf{k}_{\rm i}, \mathbf{k}_{\rm d})$ is a three-dimensional field, the third dimension ($\hat{\mathbf{z}}$) is not independent of the other two and its magnitude is given by $k_z = (\lambda^{-2} - |\mathbf{k}|^2)^{1/2}$. From equation (4), we see that equation (14) is just a convolution (in Fourier space) of the incident wavefield with the diffracted wavefield of a unit plane wave from the sample.

In Fig. 4, we introduce the coordinate systems used to simulate diffraction from the sample at the focal spot. To compute the angular spectrum of the diffracted field at the sample, $A(\mathbf{k}'_{\rm i})$, we first interpolate the incident wavefield $U_{\rm f}$ [equation (12)] into Cartesian coordinates using a piecewise cubic hermite interpolating polynomial. The angular spectrum at the focal spot $A_{\rm i}(\mathbf{k}_{\rm i})$ can then be calculated numerically using the fast Fourier transform. The wavefield $U_{\rm f}(x, y)$ is a two-dimensional slice of the incident wavefield on the focal plane, and the resulting $A_{\rm i}(k_{\rm ix}, k_{\rm iy})$ is defined strictly in two dimensions. The third component is given by $k_{\rm iz} = \{\lambda^{-2} - (k_{\rm ix}^2 + k_{\rm iy}^2)\}^{1/2}$. Finally, the coordinate system is rotated by the transformation matrix

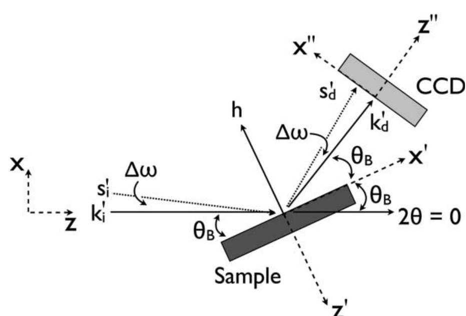

Figure 4
Sketch of coordinate systems used, with the sample and detector set at the Bragg condition. For a plane-wave component of the incident beam at an angle $\theta_{\rm B} + \Delta\omega$ to the sample surface, $\mathbf{s}'_{\rm i}$, the symmetric condition is met for a diffracted wavevector, $\mathbf{s}'_{\rm d}$, that has an angle $2\theta = 2\theta_{\rm B} + \Delta\omega$ with respect to the incident beam. On the CCD, this (symmetric) diffracted wavevector is $\Delta\omega$ from the perfect Bragg condition.

$$T = \begin{bmatrix} \sin\theta_{\rm B} & 0 & \cos\theta_{\rm B} \\ 0 & 1 & 0 \\ -\cos\theta_{\rm B} & 0 & \sin\theta_{\rm B} \end{bmatrix}$$

to obtain $A_{\rm i}(\mathbf{k}'_{\rm i})$. We can now apply equation (14) to obtain the diffracted field at the sample. For a symmetric reflection from a thin-film sample, A_h is given by equation (5) and the Dirac δ functions require $k'_{\rm ix} = k'_{\rm dx}$ and $k'_{\rm iy} = k'_{\rm dy}$ for nonzero amplitude. Therefore $k'_{\rm iz} = k'_{\rm dz}$, and equation (14) simplifies to

$$A(\mathbf{k}'_{\rm d}) \propto A_{\rm i}(\mathbf{k}'_{\rm d})\, {\rm sinc}\{\pi(2k'_{\rm dz} - h_z)t_{\rm f}\}. \qquad (15)$$

It is seen that the diffracted angular spectrum for this sample can be computed by point-wise multiplication of the incident-beam spectrum (for each diffracted-beam coordinate) with the sample diffraction function from a parallel plane wave.

To simulate the real-space diffracted wavefield as measured by the CCD, $U_{\rm SOI}(\mathbf{x}'')$, $A(\mathbf{k}'_{\rm d})$ is first rotated to the detector (double-primed) coordinate system to obtain $A(\mathbf{k}''_{\rm d})$. The real-space diffracted wavefield at the sample is $U_{\rm d}(\mathbf{x}'') = \mathcal{F}^{-1}[A](\mathbf{x}'')$, which can be propagated to the CCD by utilizing the Fraunhofer approximation since the angular Fresnel number is large. For a 124 nm thin film, we approximate the angular acceptance of the crystal α by the Scherrer equation [equation (7)]. The angular Fresnel number $Y_{\rm A} \simeq 10^5$ for $z = l_{\rm SD}$, where $l_{\rm SD}$ is the sample-to-detector distance. Thus, we apply equation (3) to yield the far-field image as measured by the CCD:

$$U_{\rm SOI}(\mathbf{x}'') \propto \mathcal{F}[U_{\rm d}]\big(\mathbf{x}''/\lambda l_{\rm SD}\big). \qquad (16)$$

Here we drop the phase terms since only the intensity is measured at the detector. Unfolding equation (16), it is clear that the real-space diffracted wavefield in the Fraunhofer approximation is just the angular spectrum of the diffracted wavefield at the sample:

$$U_{\rm SOI}(\mathbf{x}'') \propto A\big(\mathbf{x}''/\lambda l_{\rm SD}\big). \qquad (17)$$

This computation is normalized to the maximum intensity and plotted on a log scale in Fig. 5(*a*). In the figure, the two main vertical lobes of intensity correspond to the main diffraction peak, with the central portion missing because of the central stop. The ancillary intensity maxima on either side of the primary peak, in x'', correspond to the thickness fringes predicted by equation (6).

The approximate computation times for each part of the simulation based on code implemented in *Matlab 7.3* (The Mathworks Inc., Natick, USA) and run on a 2.4 GHz Intel Core 2 Quad processor are as follows: One (coarse grid) vertical slice of Fig. 2(*a*) takes 16 s, with the entire mesh plot taking approximately 1.5 h. The fine-grid vertical slice computed at the OSA that was used to continue the wavefield to the focal spot took 1 h. The diffraction computation [equation (15)] for the thin-film sample takes a few seconds. Thus within a few hours, the diffraction pattern from a kinematically scattering thin-film sample can be accurately calculated. We note here that, since the simulations conducted for this manuscript were reasonably straightforward, extensions of this formalism to asymmetric incident beams and kinema-

tically diffracting samples of finite size in three dimensions should not be formidable. These extensions are currently under investigation.

4. Experimental verification

To test the validity of the simulations presented in §3, we conducted experiments at the CNM nanodiffractometer at Sector 26-ID-C of the APS. Further details about this instrument are given by Maser, Stephenson, Shu *et al.* (2004). In our experiments the incident beam from the dual undulator source of this beamline was monochromated *via* a double-crystal Si(111) monochromator, with an energy resolution ($\Delta E/E$) of 1.7×10^{-4}, tuned to 11.2 keV ($\lambda = 1.107$ Å). This monochromatic beam was focused to nominally 30 nm by a 'staggered spoke' Xradia Au Fresnel phase zone plate (Feng *et al.*, 2007) with a 24 nm outermost zone width, a 66.5 µm radius (R_{ZP}) and a 30 µm-radius central stop (R_{CS}) (Fig. 1). The focal distance is about 29 mm from the ZP, with a depth of focus of about 10 µm and an angular divergence of 2.4 mrad. A 250 µm-thick platinum–iridium (Pt:Ir, 95:5) order-sorting aperture, with a radius (R_{OSA}) of 15 µm, is located approximately 3 mm upstream of the focal spot.

A Princeton PIXIS-XF 2-D CCD detector consisting of a 1024 × 1024 array of 13 µm square pixels was used to record X-ray intensities. At the sample-to-detector distance (l_{SD}) of 700 mm, the angular resolution is 18.6 µrad (3.83 arcseconds), with a total angular range of 19.05 mrad (1.09°). The angular resolution is probably slightly poorer because of the point spread function of the detector, which was not measured or available. However, it is unlikely that the spread is larger than ~10 µm, as a short 1:1 fiber taper is used to image the phosphor screen. As we will show in the next section, ~5 pixel resolution (~0.005°) is adequate for the purposes of this experiment; this is significantly larger than the expected point spread of the detector.

The incident-beam intensity distribution was measured at a distance of 700 mm from the focal point (Fig. 1) with the CCD normal to the zone plate axis. The measured distribution is shown in Fig. 3(*c*).

For the diffraction experiments, we used a commercially available semiconductor-grade Soitec silicon-on-insulator sample (Ying *et al.*, 2009). This sample consisted of a crystal-

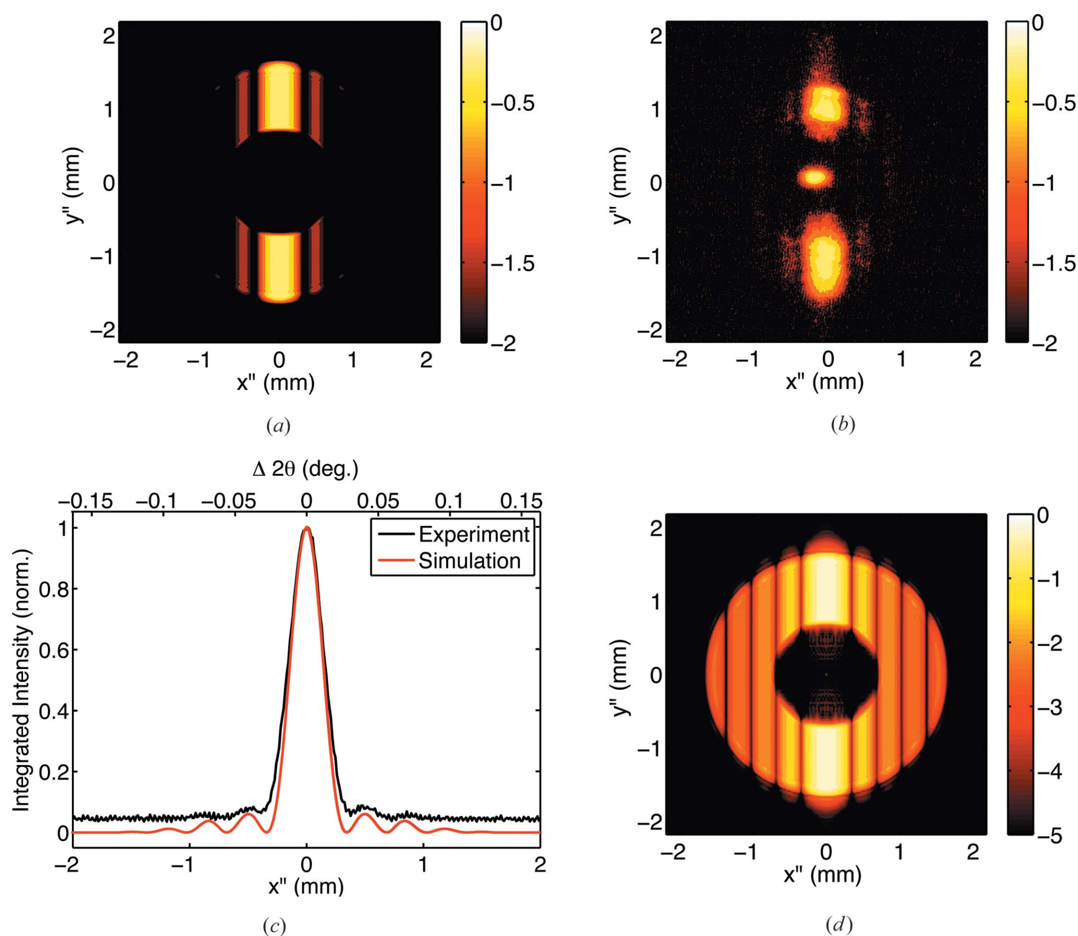

Figure 5
(*a*) Simulated thin-film diffraction from a perfect zone plate with a central stop and order-sorting aperture, normalized to the maximum intensity. (*b*) The measured 004 diffraction peak from SOI, normalized to the maximum intensity. Leakage from the central stop is seen in the center of the diffracted intensity. Both (*a*) and (*b*) are plotted on a log scale to highlight thickness fringes on either side of the main peak. (*c*) A comparison between experimental and simulated wavefield intensity integrated along $\mathbf{y}''$. (*d*) The simulated diffraction pattern plotted with a larger range of intensity.

line Si thin-film layer (the SOI layer), stacked on a 140 nm SiO_2 layer, which was on a 0.7 mm-thick Si(001)-type substrate. The film thickness of the SOI layer was measured by cross-sectional transmission electron microscopy (TEM) to be 124 (1) nm. This is an order of magnitude smaller than the extinction depth of the 004 reflection at this energy and ensured that the sample was scattering in the fully kinematical mode. Because of the bonding procedure used to make these samples, the [001] vector of the SOI layer is tilted by approximately $\sim 0.4^\circ$ with respect to the substrate [001] direction. Consequently, it was possible to measure the diffraction peak of the thin surface layer without interference from the substrate peak. The SOI 004 reflection was found by varying the sample angle θ, and detector position 2θ, to maximize the intensity measured by the CCD; the peak was found at a sample angle $\theta = 24.02^\circ$ with the CCD detector at $2\theta = 48.175^\circ$. The (two-dimensional) spatial distribution of the diffracted intensity is shown in Fig. 5(*b*). To acquire this image the CCD was exposed for 15 s and background corrected using a 15 s dark-count image.

5. Discussion and conclusions

5.1. Incident-beam profile and analysis

Both the simulated and measured incident wavefields at the CCD detector show an annulus of intensity (Fig. 3) resulting from a combination of the central stop and the divergence of the focused beam. Here both simulated and measured fields are normalized by the integrated intensity over the nonzero annulus, forcing both signals to have equal energy. While the spatial distributions of the intensities agree quite well, there are three differences that merit discussion: the experimentally measured intensity is radially asymmetric, has less sharp edges and features a bright spot at the center of the annulus.

To highlight the asymmetry in the measured incident beam (Fig. 3*c*), we plot two slices of the radial distribution along $+\hat{\mathbf{x}}$ and $-\hat{\mathbf{y}}$ in Fig. 3(*a*). The experimental data are normalized to the integrated intensity of the latter. The slice along $-\hat{\mathbf{y}}$ exhibits higher and more evenly distributed intensity than the slice in $+\hat{\mathbf{x}}$, in much better agreement with the ideal ZP simulation.

The lack of symmetry in the measured incident beam may be caused by manufacturing defects, time-dependent radiation damage to the ZP or slight misalignment of the beamline components. Our ability to model the first is impeded by the lack of information from the manufacturer of this focusing optic; the specification sheet does not include either a spatial roughness distribution or an average roughness number. A recent one-dimensional study of the roughness between zones in the ZP has shown that, provided the zones are consistent with equation (9) and the r.m.s. roughness is sufficiently small compared to the outermost zone width, the ideal ZP approximation is valid (Yan, 2009). Thus, we expect that small radially symmetric r.m.s. roughness would not qualitatively change the incident-beam intensity distribution. However, the question remains whether a two-dimensional roughness model could, at least partially, explain the asymmetry in the experimentally measured incident-beam intensity. Using the same reasoning, we did not include time-dependent radiation damage or beamline misalignment in the model since we have no data on these parameters. A detailed study of such effects is beyond the scope of this paper and will be carried out separately. At this time we can only conclude that the measured profile indicates a non-ideal focusing optic.

The smoother edges of the measured intensity in Fig. 3(*a*) are mainly due to the ZP defects discussed above. Other contributing factors to the sharper edges of the model could be diffuse scattering in the experiment, edge effects and/or approximating the 'staggered spoke' structure of the actual ZP by an ideal ZP in the simulation. While we have not accounted for these, there is still good agreement between portions of the measured incident beam and our model.

We attribute the bright spot at the center of the annulus in the experimentally measured incident-beam CCD image (Fig. 3*c*) to the use of a 'thinner-than-expected' central stop. The central stop attenuates the amplitude of the undiffracted (zeroth-order) wavefield and also adds an extra phase shift so the diffracted wavefield does not constructively interfere at the focal spot. For a thinner CS, more of the undiffracted beam would pass, resulting in a brighter spot of intensity at the CCD detector with a matching diameter (80 μm). To demonstrate this, we considered a CS with half of the thickness specified by the manufacturer. This led to a decrease of attenuation of the zeroth-order beam by a factor of 780 in the CS. The resulting wavefield at the CCD detector (dashed red line in Fig. 3*a*) does feature a bright central spot, which would illuminate only the central few pixels of the CCD.

Another phenomenon that could result in a bright central spot is the presence of higher harmonics from the dual undulator source. This is unlikely for two reasons. First, the upstream mirrors at the 26-ID-C beamline have an energy cut-off of about 12 keV and should prevent these higher-energy photons from reaching the zone plate. Second, layers of aluminium foil were used as attenuators to prevent damage to the CCD while measuring the incident beam. As the amount of attenuation was increased, the central spot intensity was observed to decrease at the same rate as the (focused) ring of intensity. We concluded that the central spot is primarily of the same energy as the focused X-rays, and any effect of the higher harmonics was secondary.

5.2. Diffracted beam profile and analysis

The simulated and experimentally measured diffraction patterns are shown in Figs. 5(*a*) and 5(*b*), respectively. In these images the x'' coordinates correspond to the 2θ direction, and the plotted intensities have been normalized by the maximum peak intensity. Qualitatively, the simulated and measured patterns look similar. In both, the central portion of the main diffraction peak is shadowed by the central stop, and thickness fringes with lower intensities bracket the main peak (in x''). There is also reasonable agreement in the real-space position, breadth and relative intensities of the peak features.

The differences between the simulated and measured diffraction patterns can be attributed to the incident-beam spectrum. The bright spot at the center of the experimental pattern is due to leakage of the zeroth-order beam through the central stop. As with the incident-beam distribution (Fig. 3*c*), the lower lobes of the diffracted signal ($y'' < 0$) are more intense than the upper lobes. These intensity artifacts are predicted by equation (15): the diffracted amplitude for a particular wavevector is just the thin-film-diffracted amplitude (from a plane-parallel wave) modulated by the incident-beam amplitude. Thus, any imperfections in the incident-beam distribution will have a linear effect on the measured diffraction signal. Interpretation of such artifacts is much easier if a test sample with a simple diffraction function is chosen.

The SOI thin-film layer is such an ideal test sample. First, the small thickness gives an angular Fresnel number that is much greater than unity. For almost any placement of detector the Fraunhofer approximation is valid for the measured diffracted intensity. Thus, while the diffracted signal measured by the two-dimensional CCD is a real-space intensity distribution, it is simply the rescaling of the diffracted angular spectrum found at the sample. For films thicker than the extinction depth, dynamical diffraction simulations may be required. As shown by Yan *et al.* (2008), the Fraunhofer approximation becomes invalid in such cases for most detector positions. This leads to complex real-space diffracted intensity distributions, especially if strain gradients are present (Yan *et al.*, 2007).

In addition to the effects from the thickness, the thin film can be considered to be infinite in the plane of the film, leading to equation (5), and subsequently equation (15). The latter explains the intensity artifacts that are found in the measured diffracted intensity that result from the incident beam. The former states that the only appreciable intensity can be measured when the difference between a diffracted- and an incident-beam vector is colinear with the reciprocal lattice vector (*i.e.* $\Delta k_{hx} = \Delta k_{hy} = 0$). For a symmetric reflection, this condition is satisfied when components of the incident and diffracted spectra make symmetric angles with the sample surface. Because of the large divergence of the incident beam and the large angular acceptance of the detector, a single CCD image contains information from the entire radial scan about the Bragg condition. However, it is not a true radial scan since each angular position on the detector does not maintain a 2:1 ratio with the (fixed) sample angle. For samples with finite lateral domains, the symmetric requirement for the incident and diffracted components is relaxed and each spatial position on the detector will contain scattered information from a range of incident-beam angular components. In these cases, distinguishing between intensity distributions from the sample *versus* incident-beam artifacts becomes nontrivial.

To obtain quantitative information from the two-dimensional diffraction patterns, the intensity along the y'' axis can be integrated at each x'' position. The resulting intensity *versus* x'' plot is equivalent to a traditional detector scan across the diffraction peak, where the slit width is given by the pixel size (or the effective pixel size corrected by the point spread function of a non-ideal CCD detector). In Fig. 5(*c*) the results of this integration, with the slit width set to 13 µm (1 pixel), are shown for both experimental and simulated data. While the resolution of the experimental curve is lower than that of the theoretical one, there is good agreement between the two curves. We note that, in the case of the experimental data, the spurious intensities within the shadow of the central stop are excluded from the integration.

For analysis of peak position and peak shape, the spatial coordinate x'' must be transformed into angular coordinates, with $\Delta 2\theta \simeq x''/l_{\rm SD}$. The angular coordinates obtained in this manner are marked on the top abscissa of Fig. 5(*c*). For the experimental intensity *versus* $\Delta 2\theta$ data, the Scherrer equation [equation (7)] yields a film thickness of 220 (6) nm, while the film thickness obtained from the period of the thickness fringes is 244 (8) nm. These values are almost double the actual film thickness measured by cross-sectional TEM. Applying these formalisms to the simulated diffraction profile yields a film thickness of 248 nm for both cases, exactly twice the input sample thickness.

The reason for this discrepancy can be understood by comparing the geometry of a traditional radial scan with the geometry of this experiment. Let us first consider the traditional radial scan with a perfect parallel plane wave incident on the sample [as used to derive equations (7) and (8)]. For a symmetric reflection at the perfect Bragg condition, both the incident and diffracted wavevectors are inclined to the sample surface by $\theta_{\rm B}$. If the sample is rotated by an amount $+\Delta\omega$ from the Bragg condition, the angle between the incident beam and the sample surface increases to $\theta_{\rm B} + \Delta\omega$. At this point, the angle between the wavevector captured by the point detector (which has not yet been moved) and the sample surface is $\theta_{\rm B} - \Delta\omega$. To maintain the symmetric geometry of the radial scan, where the incident and scattered beams make equal angles with the sample surface, the detector angle must be increased by $2\Delta\omega$. The deviation of the (symmetric) scattered vector from the perfect Bragg condition, with respect to the transmitted beam, is $\Delta 2\theta = 2\Delta\omega$. Now let us consider the geometry of this experiment. We have a divergent beam incident on a stationary sample, with the scattered intensity measured by a CCD (Fig. 4). The central axis of the incident beam makes an angle $\theta_{\rm B}$ with respect to the sample surface. For an incident-beam divergence $\alpha > \Delta\omega$, there exists a plane-wave component of the incident beam $\mathbf{s}_{\rm i}'$ that makes an angle $\theta_{\rm B} + \Delta\omega$ with respect to the sample surface. The scattered wavevector $\mathbf{s}_{\rm d}'$ that satisfies the symmetric scanning condition of the radial scan also makes this angle with respect to the sample surface. The deviation from the Bragg condition (in 2θ) is therefore $\Delta 2\theta = \Delta\omega$, half of the deviation observed in the traditional case using a sample rotation. Thus, any quantity that is measured relative to a reference value in 2θ, such as peak shifts, peak breadths or fringe periodicity, are only half as large as would be measured when sample rotations are required. Applying this coordinate correction factor of 2 to the experimental intensity *versus* $\Delta 2\theta$ data, the Scherrer equation yields a film thickness of 110 (3) nm, while the period of

thickness fringes gives 122 (4) nm. Analysis of the simulated diffraction profile yields the exact film thickness used in the simulation, 124 nm, for both methods.

In addition to this coordinate correction factor of 2, there is another difference between the traditional radial scan and the one used in this experiment: the incident wavevectors recorded at different angular positions are not equivalent. As described above, a traditional radial scan rotates the sample so that the *same* plane wave, with the *same* intensity, is incident on the sample at different angles θ. However, in the case of this experiment, different angular components of the divergent incident beam are used. It is only because the integrated intensity of the incident beam (along $\mathbf{y}''$) in the region within the FWHM of the diffraction peak is relatively constant that the Scherrer analysis gives a fairly accurate result. For incident beams with nonconstant angular intensity distributions, different 'Scherrer-like' equations can be derived.

The period of the thickness fringes, on the other hand, does not depend on the absolute intensity and yields the correct film thickness even when aberrations in peak intensity and shape occur. This technique should be preferred over the Scherrer analysis whenever possible. Thickness fringe analysis from small (perfect) domains would be enhanced by the availability of two-dimensional detectors with lower background and higher dynamic range. In our experimental data (Fig. 5*c*), the second set of thickness fringes are barely measurable above the background, while the third-order fringes are fully resolved in the simulated pattern. If we plot the simulated profile with an expanded intensity range, even more fringes become visible. This is shown in Fig. 5(*d*). If higher-resolution detectors enable the acquisition of such images, full-profile fitting of the one-dimensional compressed images could be employed for data analysis. Such analysis should take into account the presence of complete and incomplete (partially blocked) features.

We conclude that diffraction experiments using coherently focused X-ray beams *via* phase-retarding zone plates can generate complex scattering profiles even from simple samples. In particular, manufacturing defects or radiation damage in the focusing optic can add features into the diffracted signal that may be misinterpreted as originating from the sample. To obtain quantitative structural information from such images requires comprehensive full-field physics-based modeling of the relevant wavefields. Simplified one-dimensional models may not be adequate for this purpose.

6. Summary

A physics-based model that simulates a diffraction experiment with a Fresnel phase-retarding zone plate as the focusing optic, a kinematically diffracting single-crystal thin film as the specimen and a two-dimensional CCD as the detector is presented. It can be used to predict the two-dimensional wavefield at any point of the flight path of the photons. We used this model to simulate a diffraction experiment on the APS-CNM Nanoprobe instrument, and compared the simulated images with actual measurements. The results show reasonable agreement and demonstrate how forward modeling is needed for evaluation of the focusing optics and for quantitative analysis and interpretation of measurements utilizing coherent, focused beams. The formalisms presented are extendable to other geometrical configurations, and allow detailed understanding of the interaction of a focused, coherent wavefront with diffracting structures.

The authors would like to thank Mr Sean Polvino for help during the experimental measurement. The authors would also like to thank Dr Hanfei Yan and Dr Ozgur Kalenci for interesting discussions and reviewing the pre-published manuscript. BO acknowledges support from the National Science Foundation under grant No. DMS06-02235, EMSW21-RTG: Numerical Mathematics for Scientific Computing. Use of the Center for Nanoscale Materials was supported by the US Department of Energy, Office of Science, Office of Basic Energy Sciences, under contract No. DE-AC02-06CH11357. User operation of the Nanoprobe Beamline was supported by MH, JM, Robert Winarski and Volker Rose.

References

Authier, A. (2002). *Dynamical Theory of X-ray Diffraction*, IUCr Monographs on Crystallography. Oxford University Press.
Chu, Y. S. *et al.* (2008). *Appl. Phys. Lett.* **92**, 103119.
Feng, Y., Feser, M., Lyon, A., Rishton, S., Zeng, X., Chen, S., Sassolini, S. & Yun, W. (2007). *J. Vac. Sci. Technol. B*, **25**, 2004–2007.
Goodman, J. W. (1996). *Introduction to Fourier Optics*, McGraw-Hill Series in Electrical and Computer Engineering, 2nd ed. New York: McGraw-Hill.
Jones, A. R. (1969). *Brit. J. Appl. Phys.* **2**, 1789–1791.
Kang, H. C., Yan, H., Winarski, R. P., Holt, M. V., Maser, J., Liu, C., Conley, R., Vogt, S., Macrander, A. T. & Stephenson, G. B. (2008). *Appl. Phys. Lett.* **92**, 221114.
Kazimirov, A., Kohn, V. G. & Cai, Z.-H. (2009). *J. Phys. D*, **42**, 012005.
Kohn, V. G. & Kazimirov, A. (2007). *Phys. Rev. B*, **75**, 224119.
Maser, J., Stephenson, G. B., Shu, D., Lai, B., Vogt, S., Khounsary, A., Li, Y., Benson, C. & Schneider, G. (2004). *AIP Conf. Proc.* **705**, 470–473.
Maser, J., Stephenson, G. B., Vogt, S., Yun, W., Macrander, A., Kang, H. C., Liu, C. & Conley, R. (2004). *Proc. SPIE*, **5539**, 185–194.
Mimura, H., Yumoto, H., Matsuyama, S., Sano, Y., Yamamura, K., Mori, Y., Yabashi, M., Nishino, Y., Tamasaku, K., Ishikawa, T. & Yamauchi, K. (2007). *Appl. Phys. Lett.* **90**, 051903.
Schroer, C. G., Kurapova, O., Patommel, J., Boye, P., Feldkamp, J., Lengeler, B., Burghammer, M., Riekel, C., Vincze, L., van der Hart, A. & Kuchler, M. (2005). *Appl. Phys. Lett.* **87**, 124103.
Yan, H. (2009). *Phys. Rev. B*, **79**, 165410.
Yan, H., Kalenci, Ö. & Noyan, I. C. (2007). *J. Appl. Cryst.* **40**, 322–331.
Yan, H., Kalenci, O., Noyan, I. C. & Maser, J. (2008). *J. Appl. Phys.* **104**, 023506.
Ying, A. J., Murray, C. E. & Noyan, I. C. (2009). *J. Appl. Cryst.* **42**, 401–410.